Journal of
Synchrotron
Radiation

ISSN 0909-0495

Received 30 May 2008
Accepted 8 August 2008

Evaluation of the improved three-dimensional resolution of a synchrotron radiation computed tomograph using a micro-fabricated test pattern

Ryuta Mizutani,[a]* Akihisa Takeuchi,[b] Kentaro Uesugi[b] and Yoshio Suzuki[b]

[a]Department of Applied Biochemistry, School of Engineering, Tokai University, Kitakaname 1117, Hiratsuka, Kanagawa 259-1292, Japan, and [b]Research and Utilization Division, JASRI/SPring-8, Kouto 1-1-1, Sayo, Hyogo 679-5198, Japan. E-mail: ryuta@tokai-u.jp

A micro test pattern prepared by focused ion beam milling was used to evaluate the three-dimensional resolution of a microtomograph at the BL20B2 beamline of SPring-8. The resolutions along the direction within the tomographic slice plane and perpendicular to it were determined from the modulation transfer functions. The through-plane resolution perpendicular to the tomographic slice was evaluated to be 8 μm, which corresponds to the spatial resolution of two-dimensional radiographs. In contrast, the in-plane resolution within the slice was evaluated to be 12 μm. Real-space interpolation was performed prior to the tomographic reconstruction, giving an improved in-plane resolution of 8.5 μm. However, the 8 μm pitch pattern was resolved in the interpolated slice image. To reflect this result, another resolution measure from the peak-to-valley difference plot was introduced. This resolution measure gave resolution limits of 7.4 μm for the in-plane direction and 6.1 μm for the through-plane direction. The three-dimensional test pattern along with the interpolated reconstruction enables the quantitative evaluation of the spatial resolution of microtomographs.

Keywords: computed tomography; micro-CT; spatial resolution; FIB; MTF.

1. Introduction

Three-dimensional structural analysis by computed tomography is performed by recording two-dimensional images of a sample by rotating either the sample itself or the imaging system. The obtained images are subjected to reconstruction calculation giving the three-dimensional density distribution. In clinical and laboratory computed tomographs (CTs), X-ray radiation is obtained from a focused X-ray tube and used for recording radiographs. The X-ray tube gives divergent radiation called a fan beam or cone beam. In contrast, synchrotron radiation CT uses an almost parallel beam for obtaining the radiographs. The application of synchrotron radiation to tomographic analysis allowed high-resolution three-dimensional analysis at micrometer to submicrometer resolution (Bonse *et al.*, 1994; Salome *et al.*, 1999; Uesugi *et al.*, 2001; Takeuchi *et al.*, 2002). The imaging geometry and achieved spatial resolution of such high-resolution CT, hereafter called micro-CT, are very different from those of X-ray tube CT. Therefore, the resolution of the synchrotron radiation micro-CT should be evaluated from test objects appropriate for micrometer to submicrometer analyses.

The spatial resolutions of micro-CTs have been deduced from the spatial resolutions of two-dimensional radiographs. Although three-dimensional images have been used for estimating the approximate resolution of a micro-CT (*e.g.* Tang *et al.*, 2006), quantitative evaluation of the three-dimensional resolution of micro-CTs has not been performed. This is because the fabrication of three-dimensional test patterns appropriate for evaluating micrometer to submicrometer resolution is rather difficult. This paper describes the micro-fabrication of a three-dimensional test pattern by focused ion beam (FIB) milling. The spatial resolution of the micro-tomograph at the BL20B2 beamline of SPring-8 was examined using this test pattern.

According to sampling theorem, the presampling resolution can be retrieved from data sampled at a rate corresponding to twice the resolution spacing. Therefore, images for the tomographic analysis are acquired with a pixel width of less than half the spatial resolution of the two-dimensional image. The three-dimensional structure is then determined by the convolution back-projection method (Huesman *et al.*, 1977), which primarily cuts off the Fourier transform at half the frequency bandwidth. This reconstruction calculation is repeated for each tomographic slice, giving the three-dimensional structure. Therefore, the resolution in the tomographic slice, hereafter called the in-plane resolution, should be affected by the reconstruction calculation, while the resolution

along the sample rotation axis, hereafter called the through-plane resolution, is largely independent of the tomographic reconstruction. The influence of the reconstruction calculation on the in-plane resolution should be determined in comparison with the through-plane resolution.

In the study reported here, a three-dimensional micro-pattern was used for evaluating resolution from the modulation transfer function. The in-plane resolution was improved by calculating a tomogram after real-space interpolation. The improved resolution was comparable with the through-plane resolution. Another resolution measure given by the peak-to-valley difference plot is introduced, which gives a critical limit for the spatial resolution in each direction.

2. Materials and methods

2.1. Three-dimensional test pattern

A three-dimensional test pattern for the resolution evaluation was micro-fabricated by using a FIB apparatus (FB-2000, Hitachi High-Technologies, Japan) operated at 30 kV. An aluminium wire with a diameter of 250 µm was attached to the sample holder and subjected to gallium ion beam milling. A series of square wells was carved along the wire axis and along the direction perpendicular to the axis. The pitches of the resultant square-wave patterns were 16, 12, 10, 8 and 6 µm. Along the axis direction, an additional 20 µm pattern was prepared. Each pattern had a 50% duty cycle, *i.e.* 5 µm well and 5 µm interval for a 10 µm pitch. The beam aperture was selected to regulate the ion beam current. A gallium beam of 4.5 nA was used for carving the 20, 16, 12 and 8 µm patterns and a 1.7 nA beam for the 6 µm pattern, giving rectangular wells with a typical depth of 10 µm. Secondary electron images of the obtained test pattern are shown in Fig. 1. Minor defects in well shape originated from the strong beam current for carving the larger wells. The test pattern was then recovered and mounted on a stainless steel pin by using epoxy glue. Air exposure had no effect on the pattern structure.

2.2. Micro-CT

The tomographic analysis of the test pattern was performed at the BL20B2 beamline (Goto *et al.*, 2001) of SPring-8. The steel pin was mounted on the goniometer head of the micro-tomograph, using a brass fitting designed for the pin-hold sample. Transmission radiographs were recorded using a CCD-based X-ray imaging detector (AA40P and C4880-41S, Hamamatsu Photonics, Japan) and 12.000 keV X-rays. The photon flux density was determined to be 3.86×10^9 photons s^{-1} mm^{-2} at the sample position. The number of detector pixels was 2000 in the horizontal direction perpendicular to the sample rotation axis and 1312 along the vertical axis. The field of view and effective pixel size of the detector were 5.50 mm × 3.61 mm and 2.75 µm × 2.75 µm, respectively. The acquisition area, which included the test pattern image, was set to 600 × 812 pixels corresponding to an area of 1.65 mm × 2.23 mm. The images of this area were acquired with a rotation step of 0.10° and an exposure time of 600 ms per image. The data acquisition conditions are summarized in Table 1.

Table 1
Tomographic data acquisition conditions.

Beamline	BL20B2
Monochromator crystal	Si (111)
X-ray energy (keV)	12.000
Photon flux density (photons s^{-1} mm^{-2})	3.86×10^9
Pixel size (µm)†	2.75 × 2.75
Detector size (pixels)†	2000 × 1312
Detector viewing field (mm)†	5.50 × 3.61
Acquired image size (pixels)†	600 × 812
Rotation/frame (degrees)	0.10
Exposure/frame (ms)	600
Frame/dataset	1800
Dataset acquisition time (min)	90

† Width × height.

2.3. Tomographic reconstruction

The convolution back-projection method using a Hann-window filter (Chesler & Riederer, 1975; Heusman *et al.*, 1977) was used for the tomographic reconstruction. The non-interpolated reconstruction was performed with a frequency cut-off at half the total bandwidth. The filter function profile is shown in Fig. 2. For the interpolated reconstruction, the horizontal pixel strip extracted from the two-dimensional radiograph was subjected to double or quadruple linear interpolation. The double interpolation was performed by placing one additional pixel between observed pixels, and the

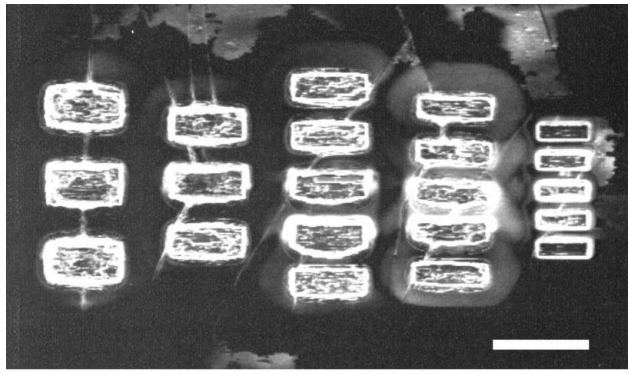

(*a*)

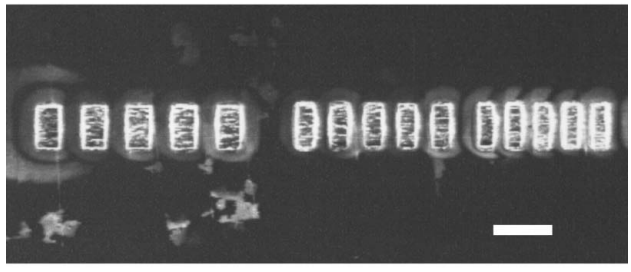

(*b*)

Figure 1
FIB secondary electron images of the micro test pattern. The wire axis is horizontal. (*a*) In-plane patterns with pitches of 16, 12, 10, 8 and 6 µm. (*b*) Through-plane patterns with pitches of 16, 12 and 10 µm. Scale bars: 20 µm.

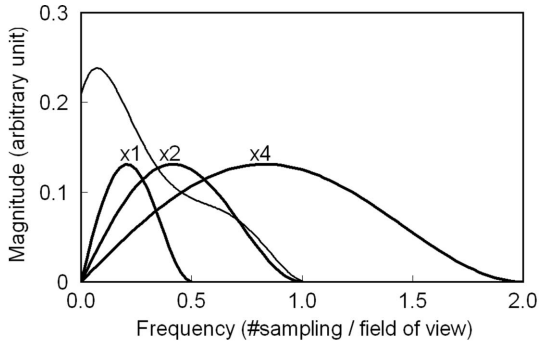

Figure 2
Filter functions for the convolution back-projection method. Profiles of the Hann-window filter (thick lines) are superposed on a schematic drawing of the Fourier transform (thin line) of the observed image strip. Filter functions for non-, double- and quadruple-interpolated reconstructions are labelled ×1, ×2 and ×4, respectively.

quadruple interpolation by placing three pixels. Each interpolated strip was subjected to a Fourier transformation. The filter functions applied to the Fourier transform of the interpolated strips are superposed in Fig. 2. Although the higher half of the frequency space was cut off, the same as in the non-interpolated reconstruction, this higher half spectra corresponds to the Fourier transform of the interpolated points and does not in principle convey the frequency information of observed data. Then the inverse Fourier transformation and back-projection calculations were performed to obtain the sample tomogram.

The periodical profile of the square-wave pattern was analyzed by taking a spatial trajectory along the test pattern. The in-plane resolution was examined from the non-, double- and quadruple-interpolated images of the pattern perpendicular to the sample rotation axis. The through-plane resolution was examined from the non-interpolated images of the pattern along the axis.

The reconstruction and examination protocols were implemented in the program *RecView* (available from http://pubweb.cc.u-tokai.ac.jp/ryuta/). Volume-rendered figures of the obtained three-dimensional structures were produced using the program *VG Studio MAX* (Volume Graphics, Germany). CT densities were rendered using the scatter HQ algorithm.

3. Results

3.1. Tomographic reconstruction

Tomographic images and spatial trajectories of the 10 µm in-plane pattern are shown in Fig. 3. Although the pattern cannot be resolved in the non-interpolated image, the double- and quadruple-interpolated images gave the periodical structure of the test pattern. The spatial trajectories of the linear absorption coefficient indicate that the double-interpolated reconstruction is sufficient for improving the spatial resolution, while the coefficients obtained from the quadruple-interpolated reconstruction gave slightly larger peak-to-valley differences than those from the double interpolation.

Tomograms of in-plane patterns obtained by the non-interpolated and quadruple-interpolated reconstruction are shown in Fig. 4. Three-dimensional renderings of the pattern structures are shown in Fig. 5. The double- or quadruple-interpolated reconstruction resolved the in-plane pattern up to a pitch of 8 µm, whereas the non-interpolated reconstruc-

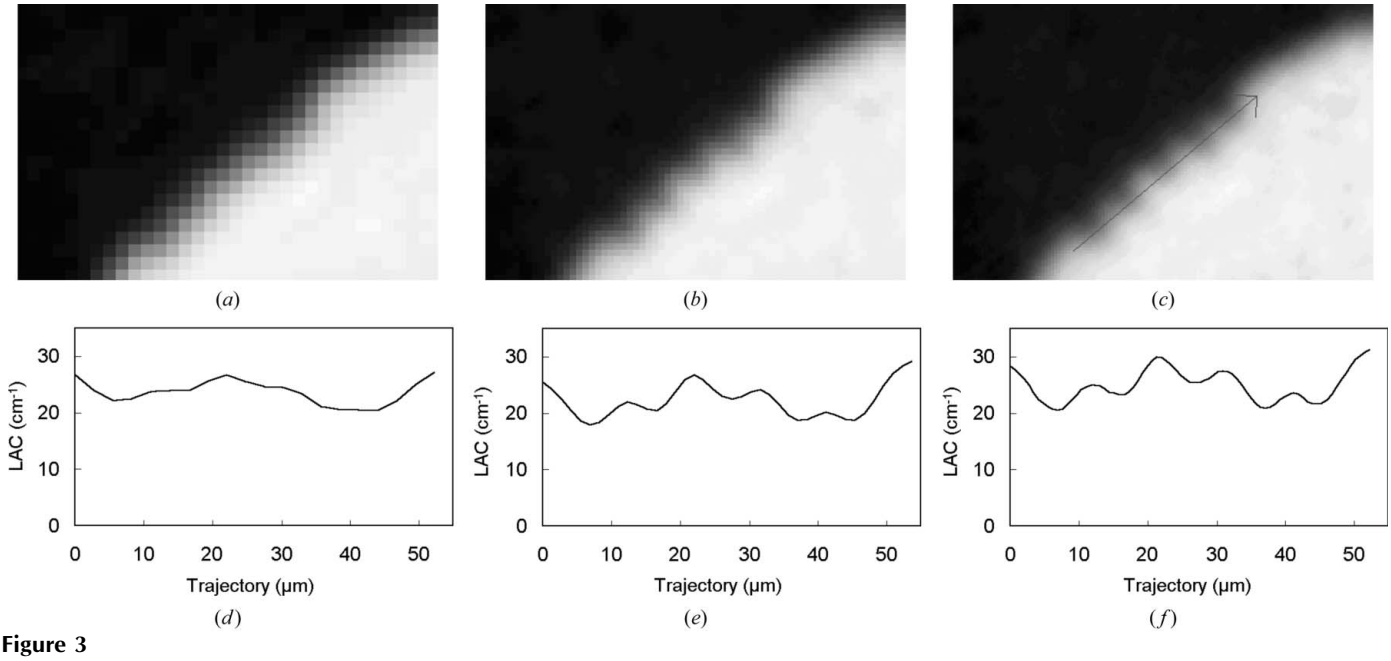

Figure 3
Tomograms and spatial trajectories of the in-plane test pattern with 10 µm pitch. Images obtained by non-, double- and quadruple-interpolated reconstruction are shown in panels (*a*), (*b*) and (*c*), respectively. Linear absorption coefficients (LACs) are shown in gray scale from 0 (black) to 38 cm^{-1} (white). LAC trajectories of non-, double- and quadruple-interpolated tomograms are shown in panels (*d*), (*e*) and (*f*), respectively. Spatial trajectories were taken along the center line of the pattern, as indicated by the arrow in panel (*c*).

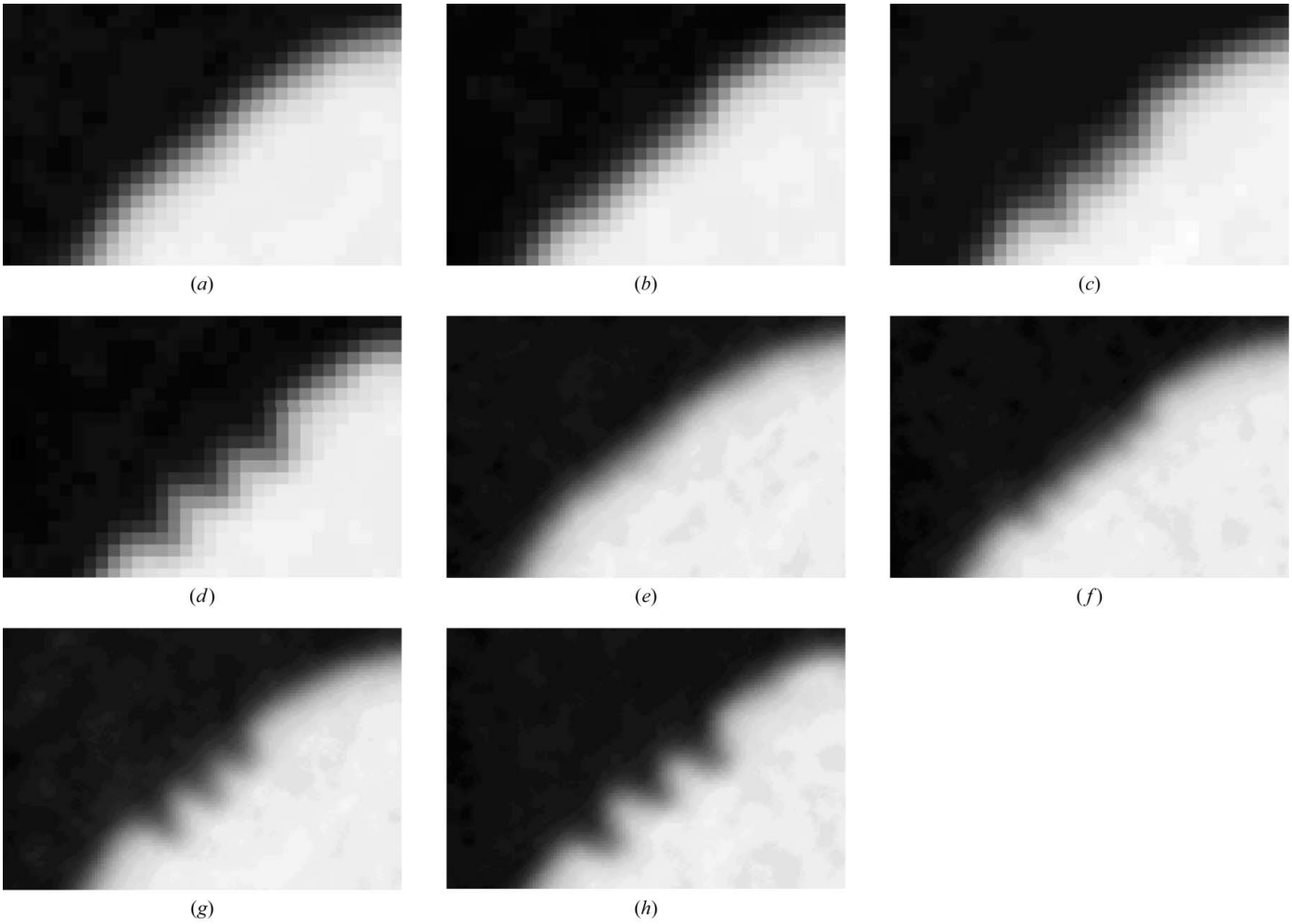

Figure 4
Tomograms of in-plane patterns obtained by (*a–d*) non-interpolated and (*e-h*) quadruple-interpolated reconstruction. (*a, e*) Pitch pattern of 6 μm; (*b, f*) 8 μm; (*c, g*) 12 μm; and (*d, h*) 16 μm. Linear absorption coefficients are shown in gray scale from 0 (black) to 38 cm^{-1} (white). Images of 10 μm pattern are shown in Fig. 3.

tion, which has been used for micro-CT analyses until the study reported here, resolved only 12 and 16 μm patterns.

The tomographic data acquisition should be performed by taking a sufficient step of $R\Delta\theta$ in the circumferential direction, where R denotes the distance from the rotation axis and $\Delta\theta$ the rotation angle per frame. The center of the in-plane pattern was located at 400 μm from the rotation axis, corresponding to the position where the circumferential step is 0.70 μm. The through-plane pattern was located at 515 μm, corresponding to a 0.90 μm step. Therefore, the circumferential step was fine enough for reconstructing tomograms of the test pattern from the observed images.

The reconstruction program used in this study was partially written in native machine language and accelerated by multi-thread processing. The convolution back-projection calculation took only 1.08 s per non-interpolated tomogram of 600 × 600 pixels on a Windows PC equipped with a 2.1 GHz Core 2 Duo processor. Although the reconstruction calculation of the double-interpolated image took three times longer than the non-interpolated image, the faster reconstruction routine implemented in this program executed the double-interpolated calculation taking only 1.5 times longer than the former non-interpolated reconstruction (Mizutani *et al.*, 2007, 2008).

3.2. Resolution evaluation

The spatial resolution can be evaluated from the peak-to-valley contrast, which is calculated from the spatial trajectory of the test pattern, as shown in Fig. 3. However, the observed contrast in linear absorption coefficients depends on the depth position of the trajectory in the carved well. A schematic drawing of observed and ideal slices of the test pattern is shown in Fig. 6(*a*). If the carved well is deep enough compared with the spatial resolution, outlines along the depth direction of the observed image coincide with those of the ideal sample structure. In such cases the peak-to-valley contrast should be virtually independent of the position of the trajectory line. The depth dependence of the peak-to-valley contrast of the in-plane 10 μm pattern is shown in Fig. 6(*b*). This depth dependence gave a plateau where the contrast was almost independent of the depth position. Therefore, the contrast can be

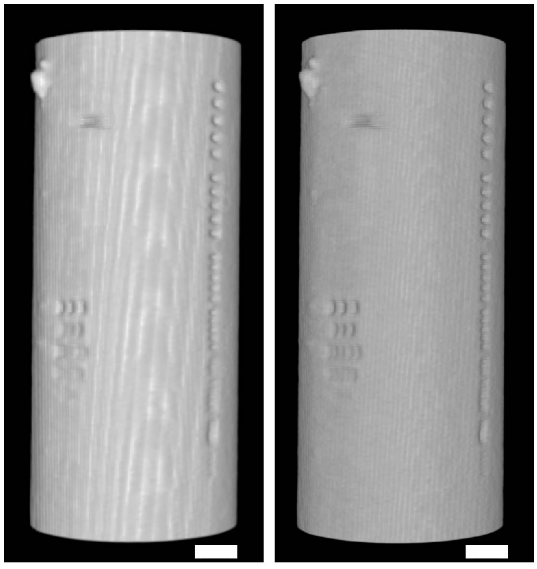

(*a*) (*b*)

Figure 5
Three-dimensional structures of the test pattern obtained by non-interpolated (*a*) and double-interpolated reconstruction (*b*). CT densities are rendered at a linear absorption coefficient of 10 cm^{-1}. Scale bars: 50 μm.

evaluated from the spatial trajectory along the mid-depth line of each carved pattern.

The ratio of the observed contrast to the intrinsic contrast between aluminium and air (41.3 cm^{-1}) was calculated separately from each pattern: the through-plane pattern and the in-plane pattern. As the spatial frequency approaches the resolution limit, this contrast transfer ratio becomes identical to the modulation transfer function (MTF). It has been reported that the contrast in the X-ray image of a square-wave test chart showed good agreement with the predicted MTF (Takeuchi *et al.*, 2001). Therefore, the contrast ratio can be treated as the MTF. Plots of this square-wave MTF in each direction are shown in Fig. 7. All the MTFs obtained from the through-plane and in-plane patterns gave positive values. The in-plane MTF plot of the non-interpolated image (Fig. 7*a*) showed a steep descent. The spatial resolution at 5% MTF was approximately evaluated to be 12 μm. This in-plane resolution is consistent with the result estimated from the tomogram of abrasives (Uesugi *et al.*, 1999). In contrast, the double- and quadruple-interpolated MTFs gave an improved resolution of 8.5 μm. This in-plane resolution is comparable with the through-plane resolution, which was evaluated to be 8 μm at 5% MTF (Fig. 7*b*). These results indicate that the double interpolation is sufficient for improving the in-plane resolution.

Although the in-plane resolution of the interpolated image was evaluated to be 8.5 μm at 5% MTF, Fig. 4(*f*) shows that the in-plane 8 μm pattern was resolved by the interpolated reconstruction. This indicates that the finer structure can be resolved in practice beyond the spatial resolution at 5% MTF. Plots of average peak-to-valley differences of the linear absorption coefficients *versus* pattern pitch are shown in Fig. 8. They indicate that the peak-to-valley difference is linearly

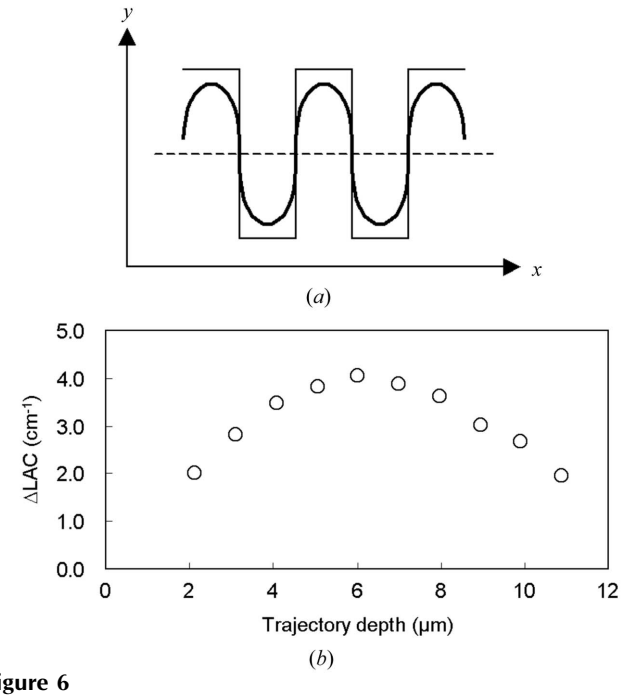

Figure 6
Evaluation of the peak-to-valley contrast. (*a*) A schematic drawing of slice images of the in-plane test pattern. Half-height contours of observed and ideal sample densities are shown by thick and thin lines, respectively. A broken line indicates a spatial trajectory where the peak-to-valley contrast is evaluated. Sample surface is to the top. (*b*) Dependence of the peak-to-valley difference on the depth position of the trajectory line. Differences in linear absorption coefficients (LACs) of the in-plane 10 μm pattern are plotted from the quadruple-interpolated image.

correlated with the pattern pitch. As discussed in Appendix *A*, the slope of the fitted line reflects the width of the point spread function. From this plot, the limit of the spatial resolution can be defined as the *x* intercept of the fitted line, giving resolution limits of 7.4 μm for the in-plane direction and 6.1 μm for the through-plane direction. These resolutions are finer than those obtained from the MTF. However, the appearance of tomograms (Figs. 3 and 4) showed agreement with the spatial resolution evaluated from the peak-to-valley difference plots rather than the resolutions from the MTF.

The spatial resolution of two-dimensional radiographs taken by the X-ray optics used in this study has been estimated to be 8 μm (Uesugi *et al.*, 1999; Mizutani *et al.*, 2008). This two-dimensional resolution corresponds to the in-plane resolution of the interpolated tomogram, but not to that of the non-interpolated tomogram. This indicates that the reconstruction calculation without interpolation did not retrieve the spatial resolution achieved by the X-ray optics, even when the radiographs were taken with the sampling theorem being taken into consideration.

4. Discussion

Quantitative evaluation of the three-dimensional resolution has not been made for the major synchrotron radiation micro-CTs. Our micro-fabricated three-dimensional test pattern along with real-space interpolation can be used to determine

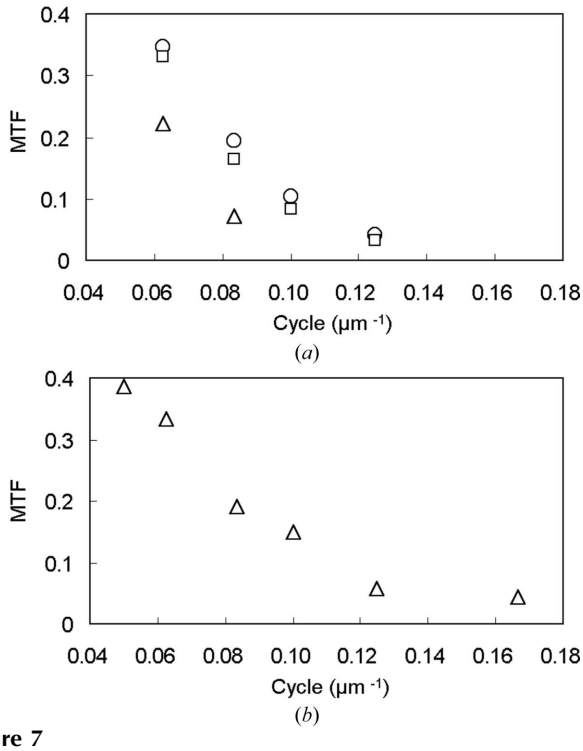

Figure 7
Square-wave MTFs calculated from in-plane (*a*) and through-plane (*b*) patterns. MTFs of non-, double- and quadruple-interpolated reconstruction are plotted with triangles, squares and circles, respectively.

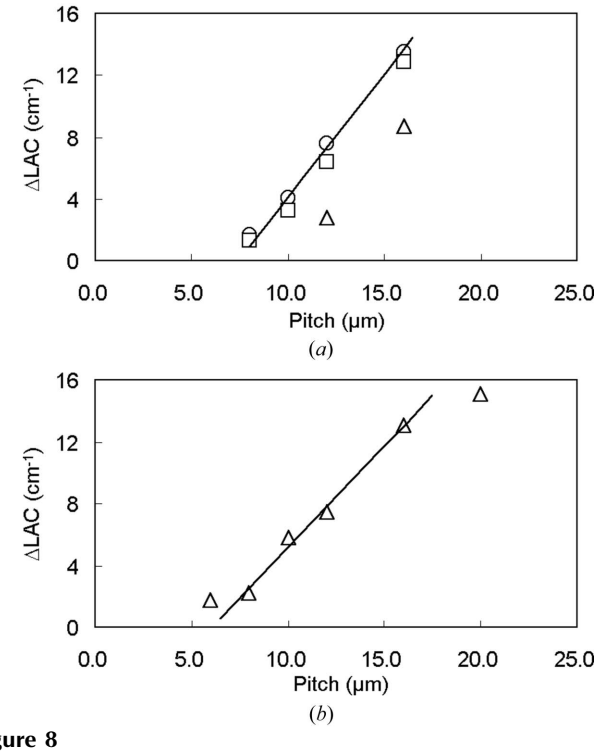

Figure 8
Average peak-to-valley difference along in-plane (*a*) and through-plane (*b*) patterns. LAC differences of non-, double- and quadruple-interpolated reconstruction are plotted with triangles, squares and circles, respectively. Solid lines are fitted to quadruple-interpolated (*a*) and non-interpolated (*b*) LACs.

the spatial resolution of any type of micro-CT. This evaluation method will give the exact resolution of the three-dimensional structure, which has not previously been determined from two-dimensional test charts.

The zoomed reconstruction has been used to obtain the point spread function of clinical CT (Mori *et al.*, 2004). In the present study the observed densities were zoomed by linear interpolation prior to the reconstruction calculation. However, the linear interpolation does not reproduce the ideal structure of the observed sample, especially around density peaks and troughs. Other interpolation methods such as quadratic models would be appropriate for precise reproduction of the sample structure.

The convolution back-projection method was performed *via* the Fourier transformation. In frequency space the real-space interpolation extends the frequency bandwidth. The filter function applied in the frequency space strengthens high-frequency structures. This would result in the linear absorption coefficients being distorted around the density edge. The spatial resolution and the density resolution countervail each other, suggesting that interpolated reconstruction should be performed only when the spatial resolution is rather important.

The spatial resolution is the fundamental parameter in the structural analysis. The three-dimensional test pattern prepared by FIB milling allowed the quantitative evaluation of the spatial resolution of the micro-CT. The machining accuracy of FIB is 100 nm or finer, so test patterns on the nanometer scale can be fabricated by FIB. Such a nanometer test pattern should allow the resolution evaluation of the nano-CTs that are planned in the major synchrotron radiation facilities.

APPENDIX *A*
Peak-to-valley difference plot

Since the tomographic image is obtained as a three-dimensional structure, the spatial resolution can be defined along arbitrary vectors in three-dimensional space. Therefore, the resolution is evaluated in one-dimensional space along the predefined measure vector, such as the in-plane or through-plane vector. Assuming that a point density in the sample is spread in the observed image by the point spread function (PSF) $f_{\rm PS}(u)$, the integral of the PSF should be

$$\int_{-\infty}^{\infty} f_{\rm PS}(u)\,{\rm d}u = 1. \qquad (1)$$

Hereafter, the PSF is considered to be symmetric about its center. The observed image $F_{\rm obs}(x)$ can be obtained by the convolution of the PSF and the ideal sample structure $F_{\rm S}(x)$ as

$$F_{\rm obs}(x) = \int F_{\rm S}(x-u) f_{\rm PS}(u)\,{\rm d}u. \qquad (2)$$

If the sample function has square waves composed of rectangular peaks with width $2w$ and density amplitude a_0 (Fig. 9), the observed density at the center of the peak is given by

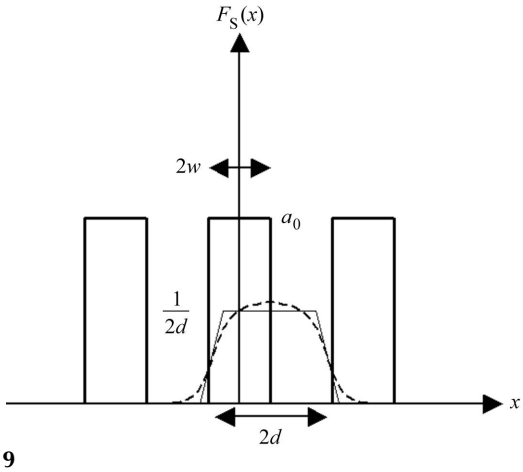

Figure 9
Ideal density distribution of the square-wave pattern with peak width of $2w$ and density amplitude of a_0. Broken lines indicate a point spread function at $x = w$. Thin lines indicate a trapezoidal approximation of the point spread function.

$$F_{\rm obs}(\text{peak}) = \int_{-w}^{w} a_0 f_{\rm PS}(u)\,{\rm d}u + \int_{3w}^{5w} a_0 f_{\rm PS}(u)\,{\rm d}u + \int_{-5w}^{-3w} a_0 f_{\rm PS}(u)\,{\rm d}u + \ldots, \quad (3)$$

where the first term corresponds to the central peak under consideration and the other terms to the distal peaks.

If the half spread of $f_{\rm PS}(u)$ is narrower than $3w$, the contributions of the distal peaks can be ignored. This assumption gives

$$F_{\rm obs}(\text{peak}) = 2a_0\big[F_{\rm PS}(w) - F_{\rm PS}(0)\big], \quad (4)$$

where $F_{\rm PS}(u) = \int f_{\rm PS}(u)\,{\rm d}u$. The integral of the symmetric PSF is 1/2 at the origin. Therefore, the center density is determined solely by $F_{\rm PS}(w)$.

Similarly, the observed density at the center of the rectangular well with width $2w$ should be

$$\begin{aligned} F_{\rm obs}(\text{well}) &= \int_{w}^{3w} a_0 f_{\rm PS}(u)\,{\rm d}u + \int_{-3w}^{-w} a_0 f_{\rm PS}(u)\,{\rm d}u + \ldots \\ &= 2a_0 \int_{w}^{\infty} f_{\rm PS}(u)\,{\rm d}u \\ &= 2a_0\big[1 - F_{\rm PS}(w)\big]. \end{aligned} \quad (5)$$

Then the peak-to-valley difference of the observed density can be obtained by

$$F_{\rm obs}(\text{peak}) - F_{\rm obs}(\text{well}) = 2a_0\big[2F_{\rm PS}(w) - (3/2)\big]. \quad (6)$$

In Fig. 8 we have fitted a line on the peak-to-valley difference plot against the pattern pitch $4w$. Since the peak-to-valley difference is proportional to the PSF integral $F_{\rm PS}(w)$, the slope of the fitted line corresponds to an average PSF height around the PSF peak. Assuming that the PSF can be approximated by a trapezoidal profile (Fig. 9) with a full width at half-maximum of $2d$, the average height of the PSF peak is estimated to be $1/(2d)$. From this approximation, the PSF integral is given by

$$F_{\rm PS}(u) \cong \frac{1}{2}\left[\frac{u}{d} + 1\right] \quad (7)$$

around the peak. When this integral is applied, equation (6) becomes

$$F_{\rm obs}(\text{peak}) - F_{\rm obs}(\text{well}) \cong a_0\left[\frac{2w}{d} - 1\right]. \quad (8)$$

This equation explains the linear correlation between the peak-to-valley difference and the pitch $4w$.

The width $2d$ corresponds to an extrapolated point where the fitted line becomes zero, $4w = 2d$. At this point the peak spreads to adjacent wells resulting in an unresolved image of the square-wave pattern. Therefore, a critical limit of the spatial resolution can be defined by this intercept $2d$ of the peak-to-valley difference plot.

Since the MTF is a Fourier transform of the PSF, the peak-to-valley difference plot is a real-space equivalent of the MTF. While the resolution evaluated from the MTF is defined by a particular threshold such as 5% MTF, the resolution from the peak-to-valley difference plot is evaluated without any threshold parameters, giving the limit of the spatial resolution.

We thank Yasuo Miyamoto, Technical Service Coordination Office, Tokai University, for helpful assistance with FIB milling. The synchrotron radiation experiments were performed at SPring-8 with the approval of the Japan Synchrotron Radiation Research Institute (JASRI) (Proposal Nos. 2007A2072 and 2007B1894).

References

Bonse, U., Busch, F., Gunnewig, O., Beckmann, F., Pahl, R., Delling, G., Hahn, M. & Graeff, W. (1994). *Bone Miner.* **25**, 25–38.
Chesler, D. A. & Riederer, S. J. (1975). *Phys. Med. Biol.* **20**, 632–636.
Goto, S., Takeshita, K., Suzuki, Y., Ohashi, H., Asano, Y., Kimura, H., Matsushita, T., Yagi, N., Isshiki, M., Yamazaki, H., Yoneda, Y., Umetani, K. & Ishikawa, T. (2001). *Nucl. Instrum. Methods Phys. Res. A*, **467–468**, 682–685.
Heusman, R. H., Gullberg, G. T., Greenberg, W. L. & Budinger, T. F. (1977). *RECLBL Library Users Manual: Donner Algorithms for Reconstruction Tomography.* Lawrence Berkeley Laboratory, University of California, USA.
Mizutani, R., Takeuchi, A., Hara, T., Uesugi, K. & Suzuki, Y. (2007). *J. Synchrotron Rad.* **14**, 282–287.
Mizutani, R., Takeuchi, A., Uesugi, K., Ohyama, M., Takekoshi, S., Osamura, R. Y. & Suzuki, Y. (2008). *Brain Res.* **1199**, 53–61.
Mori, S., Endo, M., Tsunoo, T., Kandatsu, S., Tanada, S., Aradate, H., Saito, Y., Miyazaki, H., Satoh, K., Matsushita, S. & Kasakabe, M. (2004). *Med. Phys.* **31**, 1348–1356.
Salome, M., Peyrin, F., Cloetens, P., Odet, C., Laval-Jeantet, A. M., Baruchel, J. & Spanne, P. (1999). *Med. Phys.* **26**, 2194–2204.
Takeuchi, A., Takano, H., Uesugi, K. & Suzuki, Y. (2001). *Proc. SPIE*, **4499**, 29–37.
Takeuchi, A., Uesugi, K., Takano, H. & Suzuki, Y. (2002). *Rev. Sci. Instrum.* **73**, 4246–4249.
Tang, M.-T., Yin, G.-C., Song, Y.-F., Chen, J.-H., Tsang, K.-L., Liang, K. S., Chen, F.-R., Duewer, F. & Yun, W. (2006). *IPAP Conf. Ser.* **7**, 15–17.
Uesugi, K., Suzuki, Y., Yagi, N., Tsuchiyama, A. & Nakano, T. (2001). *Nucl. Instrum. Methods Phys. Res. A*, **467–468**, 853–856.
Uesugi, K., Tsuchiyama, A., Nakano, T., Suzuki, Y., Yagi, N., Umetani, K. & Kohmura, Y. (1999). *Proc. SPIE*, **3772**, 214–221.